

ARTICLE OPEN



Data-driven analysis of process, structure, and properties of additively manufactured Inconel 718 thin walls

Lichao Fang ^{1,4}, Lin Cheng ^{1,4}, Jennifer A. Glerum², Jennifer Bennett ^{1,3,5}, Jian Cao ¹ and Gregory J. Wagner ¹

In additive manufacturing of metal parts, the ability to accurately predict the extremely variable temperature field in detail, and relate it quantitatively to structure and properties, is a key step in predicting part performance and optimizing process design. In this work, a finite element simulation of the directed energy deposition (DED) process is used to predict the space- and time-dependent temperature field during the multi-layer build process for Inconel 718 walls. The thermal model results show good agreement with dynamic infrared images captured in situ during the DED builds. The relationship between predicted cooling rate, microstructural features, and mechanical properties is examined, and cooling rate alone is found to be insufficient in giving quantitative property predictions. Because machine learning offers an efficient way to identify important features from series data, we apply a 1D convolutional neural network data-driven framework to automatically extract the dominant predictive features from simulated temperature history. Very good predictions of material properties, especially ultimate tensile strength, are obtained using simulated thermal history data. To further interpret the convolutional neural network predictions, we visualize the extracted features produced on each convolutional layer and compare the convolutional neural network detected features of thermal histories for high and low ultimate tensile strength cases. A key result is the determination that thermal histories in both high and moderate temperature regimes affect material properties.

npj Computational Materials (2022)8:126; https://doi.org/10.1038/s41524-022-00808-5

INTRODUCTION

Metal additive manufacturing (AM) is a technology that can be used to build parts layer-by-layer, allowing the fabrication of parts with more complex geometry and reduced costs compared with traditional manufacturing techniques^{1,2}. Directed energy deposition (DED) is one popular metal additive manufacturing process³ in which metal powder is delivered by one or more nozzles⁴. A focused heat source, such as a laser, is used to melt the injected metal material locally. Parts are built progressively as each layer is scanned and melted in a predetermined pattern.

During the DED process, parts undergo repetitive thermal heating and cooling cycles due to the deposition of multiple layers. The resulting complex thermal field in parts, both during and after solidification, has significant effects on the final material microstructure and mechanical properties, such as yield stress, yield strain, ultimate tensile strength (UTS), and failure stress^{5–7}. However, it is time-consuming and expensive to conduct DED experiments to optimize process parameters and tool paths for a given geometry to yield parts with good mechanical properties. Computational models can be an efficient approach to obtaining temperature histories of parts, which can be related to the microstructure and mechanical properties.

To predict the thermal field, many researchers have used the finite element method to solve the heat equation and simulate the transient temperature field in AM. For most DED thermal models, the boundary condition on the outer part surface assumes convection with a constant convection coefficient^{8–15}. However, DED processes typically include a forced shield gas flow, with a flow velocity that varies over the part surface; therefore, a spatially varying convection coefficient model calibrated against measured

thermocouple data have been proposed and showed a better match with experimental temperature histories compared with a uniform convection coefficient model³.

Calibrations of thermal DED models are also challenging. Almost all previous calibrated thermal models for multi-layer deposition have been based on thermocouple measurements taken far from the laser spot 16-18. However, it is difficult to directly measure the temperature in or near the melt pool region with thermocouples because of the extreme temperature range and the constantly changing geometry. Alternatively, dynamic infrared (IR) images measured by IR cameras have been used to calibrate thermal models^{19,20}. An IR camera can capture the emitted thermal radiation at the part surface, including near the melt pool, providing a complement to thermocouple data for calibrating and validating thermal models^{19–25}. For instance, IR images have been captured to verify a moving heat source thermal model for induction-assisted weld-based additive manufacturing (WAM)¹⁹. IR cameras have also been used to calibrate the thermal model for a single pass multi-layer gas metal arc welding (GMAW) process²⁶: this work only studied two layers of deposition rather than a full part-scale model.

Nickel-based alloys, such as Inconel 718, have been widely used in AM applications (e.g., turbine blades and combustion chambers) because of their excellent tensile strength, high-temperature yield strength, creep properties, and corrosion resistance^{6,27–30}. Mechanical properties are found to depend not only on grain size and microstructure orientation, but also on the precipitate distribution of the material^{7,28}. For example, Laves phases are brittle precipitates in Inconel 718 usually formed during Nb segregation in the inter-dendrite regions in solidification. Laves

¹Department of Mechanical Engineering, Northwestern University, Evanston, IL 60208, USA. ²Department of Materials Science and Engineering, Northwestern University, Evanston, IL 60208, USA. ³DMG MORI, Hoffman Estates, IL 60192, USA. ⁴Present address: Department of Mechanical and Materials Engineering, Worcester Polytechnic Institute, Worcester, MA 01609, USA. ⁵Present address: Department of Civil and Mechanical Engineering, US Military Acadeemy at West Point, West Point, NY 10996, USA. [™]email: gregory.wagner@northwestern.edu





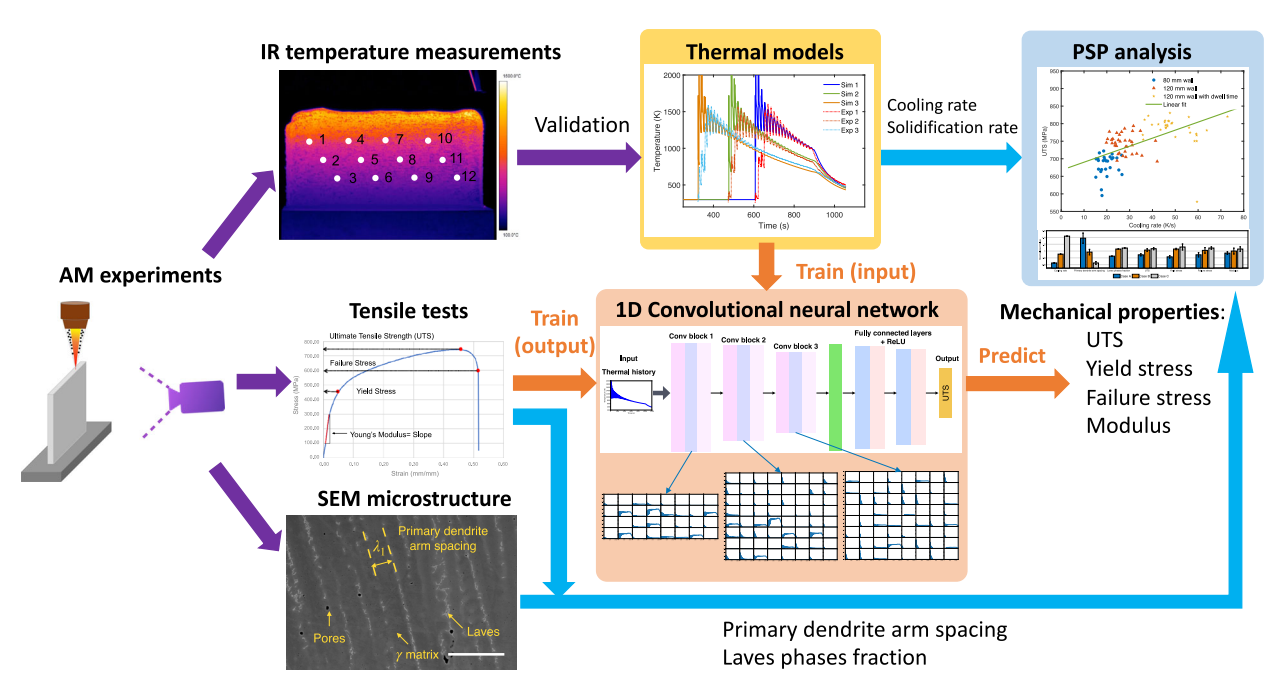


Fig. 1 Overview of the data-driven analysis for process-structure-properties. The 1D convolutional neural network is used to predict mechanical properties from simulated thermal history. The simulated thermal process data, microstructure, and measured mechanical properties are analyzed for process-structure-properties (PSP) relationship.

phases can reduce the mechanical properties of the material, such as lowering the yield strength and Young's modulus for Inconel 718²⁸. The microstructure can be affected by the chemical composition and thermal conditions during the AM process²⁹. Therefore, it is important to investigate the detailed effects of thermal history on microstructure and mechanical properties.

Much previous work uses cooling rate to describe the relationship between temperature, microstructure, and properties. Researchers have found that cooling rate influences grain size, dendrite arm spacing, microsegregation, precipitate formation^{22,31,32}, anisotropy, porosity, and strength²¹. High cooling rates can lead to faster solidification that results in finer microstructure and enhanced mechanical properties³³. However, far less previous work investigates whether cooling rate is the only important factor for microstructure and mechanical properties. It has been found that the combination of thermal gradients, cooling rates (the average rate of temperature change during solidification, in units of temperature per time), and solidification rates (the speed of the solidification front, in units of length per time) can influence the liquid-solid interface stability and then affect the dendrite arm spacing and final properties^{30,34,35}. However, the complex thermal effects on microstructure and mechanical properties are not fully understood. This motivates us to develop a method to automatically extract features from temperature history and investigate the correlation between thermal history and mechanical properties.

Machine-learning techniques provide an effective way to extract information from a signal or time series. For example, a convolutional neural network (CNN) can learn local patterns from input data through convolutions without a priori feature selection^{36–39}. CNNs have been highly successful in many applications, such as speech recognition, self-driving vehicle control, and computer vision^{39–41}. Recently, one-dimensional (1D) CNNs have been used to extract features from 1D input data, such as a heart signal or other time-series data^{40–45}. CNNs can learn local features from raw data, and then extract more global and high-level features in deeper convolutional layers^{40,42,46}. Measured or simulated thermal history data from DED-built parts can be regarded as a dynamic time series. Recently, it was shown that a

2D CNN can be used to correlate the experimentally measured thermal history in AM with material properties⁴⁷. Xie et al.⁴⁷ used raw uncalibrated IR measurements as the thermal histories and applied wavelet transform to convert the IR signals to 2D wavelet scalograms. Then the authors applied a 2D CNN model to predict UTS from the 2D wavelet scalograms, and used a random forest model to analyze the influence of temperature on properties. However, using experimentally measured IR data in data-driven models is restrictive; accurate IR measurements require careful calibration of material emissivity, and can only be gathered at surfaces, making IR measurement difficult or impossible for complex geometries. In the current work, instead of using measurements as the input to our data-driven model, we develop a validated thermal model to predict thermal histories. We apply a 1D CNN model to automatically extract features from simulated temperature history and predict mechanical properties. Since correlations discovered by CNNs can be difficult to interpret 46,48,49 in this work we visualize the intermediate convolutional layers and compare the extracted features of entire thermal histories using CNNs for high and low UTS cases. The proposed data-driven framework can help to investigate thermal effects on mechanical properties and improve understanding of the underlying physics in the process.

In this work, a combination of the validated computational thermal model, together with a data-driven method based on a 1D CNN, is developed to accurately simulate the process and use the entire time-dependent temperature curve to predict mechanical properties throughout the final part. The overview of the datadriven model framework is shown in Fig. 1. First, we use a thermal model based on the finite element method with spatially varying surface convection for the DED multi-layer build process of Inconel 718 material. Three cases with different domain sizes and dwell times are investigated. The thermal model is validated using IR images from in situ DED experiments. Microstructure characterization and tensile tests are also conducted for selected material samples. Then, a 1D CNN is used to extract features from simulated thermal histories to predict mechanical properties. The correlation between thermal history, microstructure, and mechanical properties is investigated and discussed. To better understand

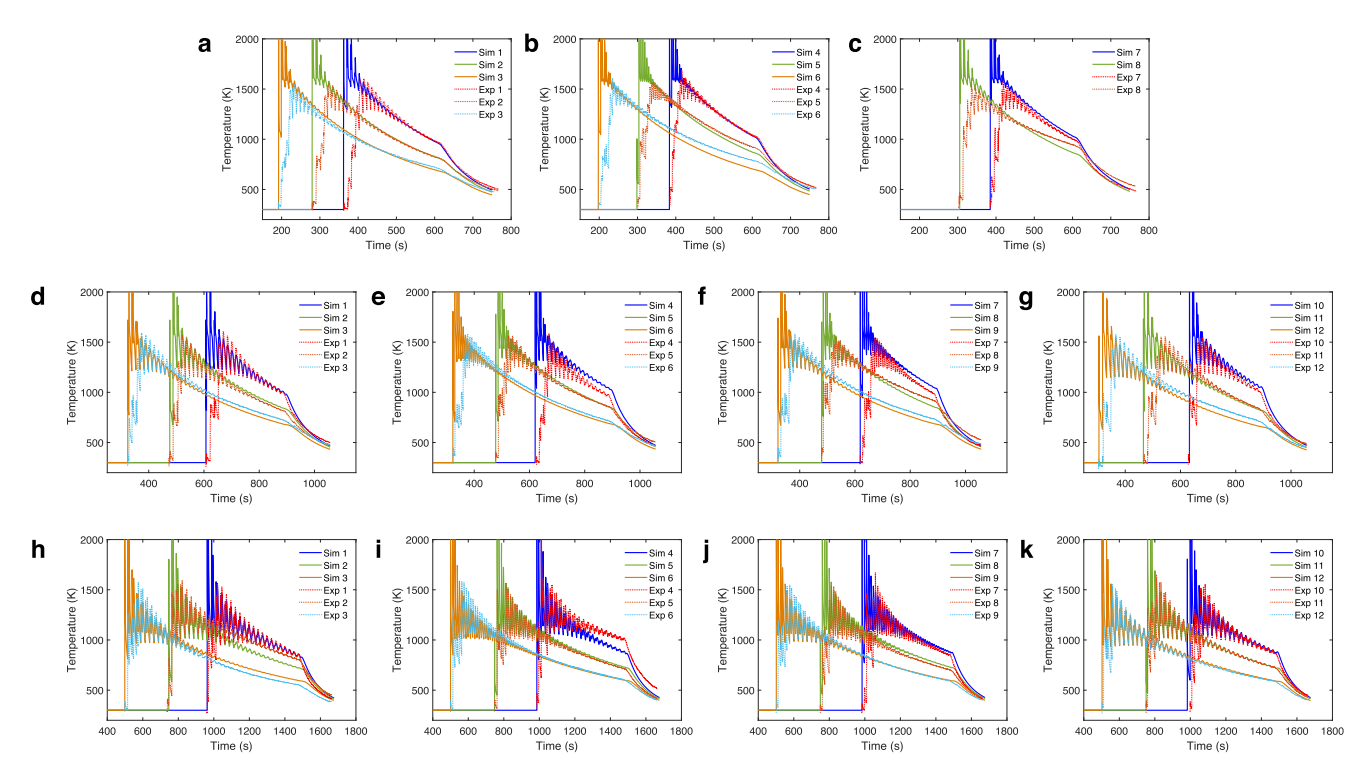


Fig. 2 Comparison of simulated and experimental temperature histories. a–c Case A, 8 specimen locations. d–g Case B, 12 specimen locations. h–k Case C, 12 specimen locations. An enlarged view of h is provided in Supplementary Fig. 2 for clarity. Point locations are labeled in Supplementary Fig. 1d and e.

the physical mechanism, we visualize the extracted features from intermediate convolutional layers to interpret the correlation between thermal histories and properties. We analyze the distinction in the CNN-detected features between multiple high and low UTS cases to investigate the contribution of thermal history to different UTS. This work demonstrates an efficient way to simulate the thermal history of DED deposition, predict properties from such a thermal history by 1D CNN, and further understanding of thermal effects on solidification and mechanical properties.

RESULTS

Thermal simulation and validation

In this work, three cases of thin wall, multi-layer depositions, during the DED process are simulated using the computational thermal model (see the "Methods" section). The three cases are 80 mm walls with 0 s dwell time (Case A), 120 mm walls with 0 s dwell time (Case B), and 120 mm walls with a 5 s inter-layer dwell time (Case C). More details of the three cases are listed in Supplementary Table 1. The schematic of the DED process is shown in Supplementary Fig. 1a. The bidirectional tool path used in the simulation and experiment is shown in Supplementary Fig. 1b. For the simulation, the geometry of the computational domain and meshes are shown in Supplementary Fig. 1c. The top part of the domain is the thin Inconel 718 wall while the bottom part is the stainless steel 304 substrate. More process parameters and thermal-physical properties of material Inconel 718 and substrate material stainless steel 304 are listed in Supplementary Tables 2, 3, and 4.

The model computes temperature as a function of time and space. Detailed temperature history is output at every time step for each specific probe point. To investigate the correlation between thermal history and mechanical properties, we choose the probe points in the simulation at the same locations as the

experimental tensile test coupons. Further post-processing of the temperature solutions provides additional data used for analysis (see "Methods"). The proposed computational model can efficiently provide thermal history, cooling rate, and solidification rate to further investigate the correlation between thermal data, microstructure and mechanical properties.

The parameters in the spatially varied heat convection model, the laser absorption efficiency, and the emissivity values in the model are calibrated using the thermal history measured by the IR camera in the experiment. Figure 2 shows the temperature histories predicted by the calibrated computational models compared with experiments for Cases A, B, and C, respectively. The locations of point 3 through 8 for Case A and 1 through 12 for Cases B and C are labeled in Supplementary Fig. 1d and e.

The results show that the predicted thermal history agrees well with the experimental results for most specimen locations. For example, Fig. 2a shows a comparison of the thermal histories from simulation (solid lines) and experimental IR camera data (dashed lines) for points 1, 2, and 3 in Case A during the DED process. The initial temperature is the ambient temperature of 295 K. At around 200 s, the temperature of point 1 increases when the laser starts to scan at that location.

However, there are some discrepancies between the simulated and measured data during this initial increase. The measured temperature increases more slowly than the simulation and notably does not exceed the solidus temperature of the material (1533 K), which is incorrect. In addition, in the IR images in Supplementary Fig. 1d and e, the top surface, especially the melt pool right under the laser source, appears cooler than some of the previously built layers. This failure to measure the temperature of the molten material is attributed to the difference in emissivity between the liquid and solid phases of the material²⁶. The emissivity of liquid metal alloys is much lower than that of solid metal alloys, leading to erroneously low-temperature measurements in the melt pool. Near and above the solidus temperature,



therefore, the simulated temperatures are considered more reliable than experimental data. To improve the accuracy of the measured temperature, methods for calibrating emissivity for liquid and solid metal alloys should be developed in the future. Simulation accuracy may be impacted through a more detailed characterization of the true part boundary conditions, especially the heat convection over the entire surface.

After the simulated temperature decreases below the solidus temperature, the simulated and experimental curves match well. The rapid oscillation of each temperature curve is caused by the multiple passes of the laser as additional material is added; both the mean and the amplitude of the oscillations decrease as the wall grows in height and the amount of material between the point and the laser spot increases. The laser source is turned off around 615 s in Fig. 2a, after which both the simulated and experimental curves decrease more quickly and monotonically. (There is a slight delay in the onset of faster temperature decrease of about 5-10 s between each row of points due to the thermal diffusion time; this delay is difficult to detect in the plots because of the scale of the temperature axes.) The cooling rate during this final period is mainly determined by free convection and radiation at the wall and substrate surfaces. Trends of thermal histories are similar in Fig. 2b-k. An enlarged view of the temperature curve for Case C with locations of 1, 2, and 3 is provided in Supplementary Fig. 2 for clarity.

Microstructure analysis

The microstructure of DED thin walls is observed by the scanning electron microscope (SEM). The SEM-imaged microstructure for samples from the 80 mm thin wall, 120 mm thin wall, and 120 mm thin wall with a dwell time of 5 s (Cases A, B, and C) are shown in Fig. 3a–f. The locations for the probed points in the three different thin-wall parts are (x, z) = (8.3, 34.6) mm, (15.0, 32.8) mm, and (15.1, 39.3) mm, respectively, where the (x, z) = (0, 0) point is taken as the lower-left corner of thin walls in Supplementary Fig. 1d and e. The simulated temperature is recorded at the center through the thickness of each sample location. Microstructure SEM samples are imaged from the side view (normal to the scan direction, i.e., the y-z plane) and top view (normal to the build direction, i.e., the x-y plane). From the SEM images, we can see the y matrix phase, the Laves phases, and a few δ phases (black dots inside of Laves phases). Laves phases are often observed to precipitate at grain boundaries. The δ (Ni₃Nb) phases usually precipitate along grain boundaries and within the intergranular matrix. Both Laves phases and δ phases are detrimental to mechanical properties⁵⁰. We can also observe defects forming in the microstructure, such as pores shown in Fig. 3d. The formations of pores are highly related with thermal histories and affect the mechanical properties of the part. Using the image processing software ImageJ⁵¹, we calculated the volume fraction of Laves phases and primary dendrite arm spacing for the top and side view of microstructures in the three thin walls shown in Supplementary Tables 5 and 6.

Process and location effects on the cooling rate, microstructure, and mechanical properties

We compare cooling rates, microstructure features (primary dendrite arm spacing and the volume fraction of Laves phases), and experimentally measured mechanical properties (UTS, yield stress, failure stress, and modulus) in Supplementary Table 5 for three cases. These values are plotted in Fig. 3g, normalized by the mean value across the three cases. The primary dendrite arm spacing is measured by calculating the mean value of several primary dendrite arm spacings in the SEM images in Fig. 3. The 80 mm wall (Case A) has the largest primary dendrite arm spacing, while the 120 mm wall with 5 s dwell time (Case C) has the smallest. Error bars based on the standard deviation across

measurements of repeated experiments are also shown in Fig. 3g. The cooling rate is calculated based on the thermal history of a single location on the wall (see Methods). Volume fractions of Laves phases are calculated based on the single SEM image of the sample. From the figure, we can see that Case C, with the highest cooling rate, has the finest grains and relatively high strength (UTS, yield stress, failure stress, and modulus), while Case A, with the lowest cooling rate, has coarser grains and lower strength. We can conclude that increasing the time between successive laser scans, whether by increasing the wall size or the dwell time, increases the cooling rate and leads to finer microstructures and higher strength.

We also investigate variations in microstructure and properties at different locations in the same wall. Top and side views of the microstructure are imaged at three different locations for Case B in Fig. 4a-f. Specimen locations are shown in Supplementary Fig. 3; point 1 is closer to the top of the wall, point 8 is in the middle, and point 12 is near the bottom. Primary dendrite arm spacing and Laves phases volume fraction are calculated from the SEM images in Fig. 4 via ImageJ and listed in Supplementary Table 6 along with the cooling rate, yield stress, UTS, failure stress, and modulus. These values, normalized by their means, are plotted in Fig. 4g. In the SEM images, some circular (presumably spherical) and irregular black pores are seen in Fig. 4a-f. The formation of both spherical and irregular pores are expected to be highly related to temperature history as demonstrated in our prior work⁵². Spherical pores may be caused by the evaporation of metal elements in the melt pool, usually when laser scan speed is not fast, while irregular pores are induced by lack of fusion. The formation of pores leads to the reduction of the load-bearing cross-sectional area during the tensile test, which usually results in a lowered measured strength^{53,54}.

From Fig. 4g, we see no clear correlation between cooling rate, microstructure, and mechanical properties. The middle location has larger primary dendrite arm spacing than the top and bottom specimen. From bottom to top, the primary dendrite arm spacing gradually increases but then decreases. The trend is the same with the volume fraction of Laves phases and mechanical properties. But cooling rate decreases monotonically from top to bottom of the wall although the differences in cooling rate between the three locations are small. These results indicate that the cooling rate alone is insufficient to predict mechanical properties for different locations in one wall. Other thermal history features may be needed to develop correlations between process and mechanical properties.

Prediction of primary dendrite arm spacing

The relationship between measured primary dendrite arm spacing and simulated cooling rate for samples from different cases and locations is shown in Fig. 5a. The primary dendrite arm spacing is measured from the 12 SEM microstructure images with different locations in different cases. The simulated cooling rates are also calculated at the corresponding locations. The primary dendrite arm spacing, simulated cooling rates, and locations for the 12 samples are tabulated in Supplementary Table 7. The dotted line in Fig. 5a is the linear fit to the data with the R^2 error of 0.81:

$$\lambda_1 = -0.26\dot{T} + 19.60 \tag{1}$$

where λ_1 is the primary dendrite arm spacing (μ m) and \dot{T} is the cooling rate (K s $^{-1}$). Results indicate a strong correlation between primary dendrite arm spacing and cooling rate. It shows that increasing cooling rate leads to smaller dendrite arm spacing, which is in agreement with previous findings^{28,55}.

According to solidification theory³⁴, primary dendrite arm spacing is closely related to thermal gradient and solidification rate. To understand the relationship between the primary dendrite arm spacing, thermal gradient and solidification rate,

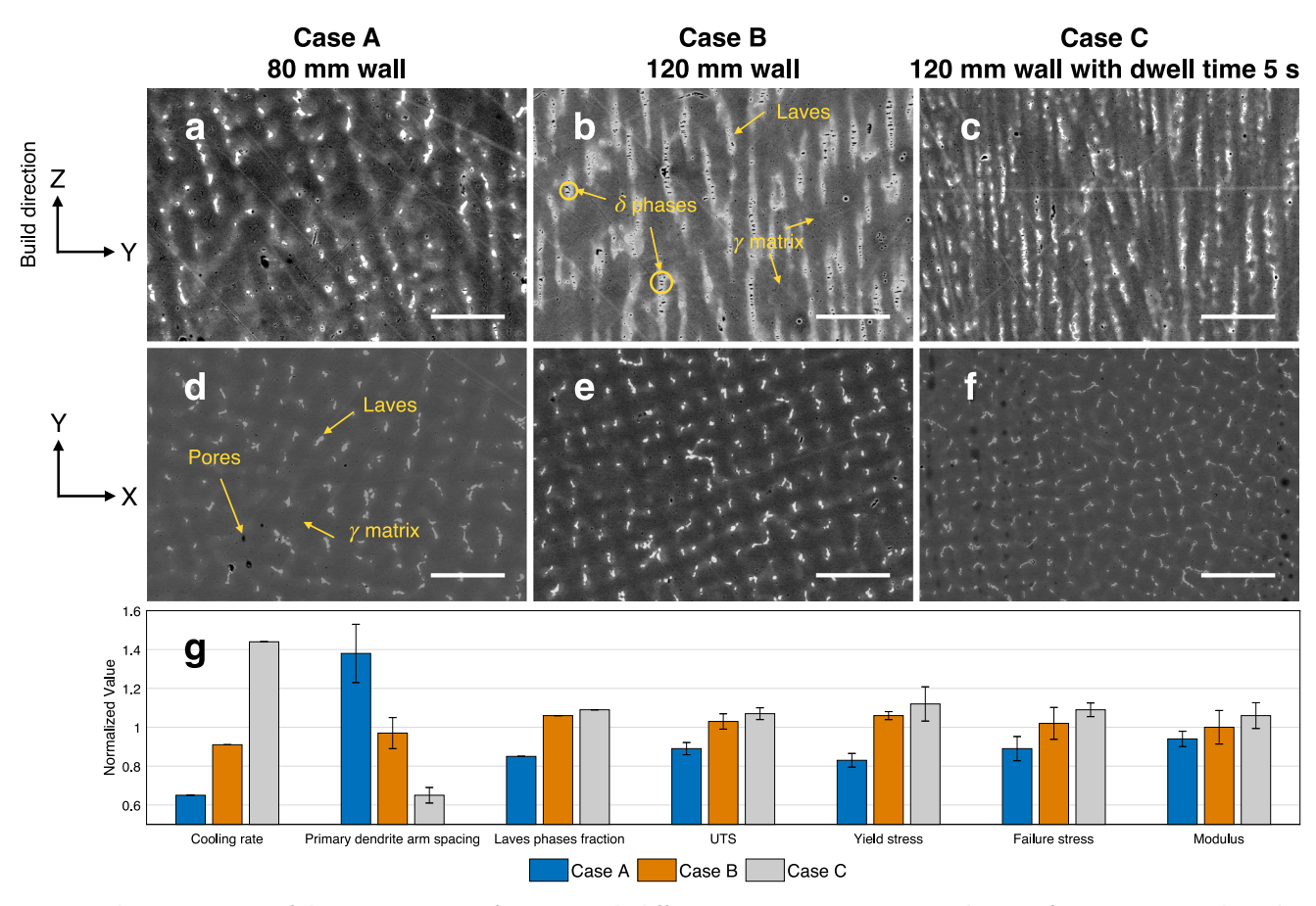


Fig. 3 SEM characterization of the microstructure for parts with different process parameters. High magnification images $\bf a$, $\bf b$, and $\bf c$ are the side view (normal to the scan direction) of samples from the three cases, while $\bf d$, $\bf e$, and $\bf f$ show the top view (normal to the build direction). The locations of probed points are (x,z)=(8.3,34.6) mm, (15,32.8) mm and (15.1,39.3) mm for Case A, B, and C respectively. Some original SEM images ($\bf a$ - $\bf c$) are reprinted from ref. The parameters of computed cooling rate, microstructure, and mechanical properties of different thin walls. Values are tabulated in Supplementary Table 5 normalized by the mean across the three cases. The error bars for primary dendrite arm spacing, UTS, yield stress, failure stress, and modulus give standard deviations of repeated experiments. Cooling rate and volume fractions of Laves phases are calculated based on a single simulation and measurement and therefore have no standard deviation reported. The scale bars in ($\bf a$ - $\bf f$) are 40 μ m.

we compared our data with the analytical model of Kurz and Fisher³⁴:

$$\lambda_1 = A(\Gamma \Delta T_0 D_{\ell}/k)^{0.25} G^{-0.5} V_s^{-0.25}$$
(2)

where λ_1 is the primary dendrite arm spacing (m), A is a fitting coefficient, Γ is the Gibbs-Thomson coefficient ($\Gamma=3.65\times 10^{-7}$ K m), ΔT_0 is the undercooling ($\Delta T_0=T_I-T_s$, the unit is K), D_ℓ is the diffusion constant in the liquid (m² s $^{-1}$), k is the partition coefficient ($k=0.48^{56}$), G is the thermal gradient (K m $^{-1}$), and V_s is the solidification rate (m s $^{-1}$). The thermal gradient and solidification rate are calculated from the simulation data (as described in "Methods") while the primary dendrite arm spacing is measured from experiments. We calculate the value of A from the best fit to our experimental data using the Kurz and Fisher model. The final form of the Kurz and Fisher model based on our sample data is

$$\lambda_1 = B G^{-0.5} V_s^{-0.25} \tag{3}$$

where the coefficient $B = A(\Gamma \Delta T_0 D_\ell/k)^{0.25} = 4.40 \times 10^{-4} K^{0.5} \, m^{0.75} \, s^{-0.25}$. The R^2 error of the Kurz and Fisher model based on the data is 0.47.

We also fit the data to an expression that is linear in $G^{-0.5}V_s^{-0.25}$:

$$\lambda_1 = C_1 G^{-0.5} V_5^{-0.25} + C_2 \tag{4}$$

where the coefficient $C_1 = 1.41 \times 10^{-3} \text{K}^{0.5} \text{ m}^{0.75} \text{ s}^{-0.25}$, and $C_2 = -2.62 \times 10^{-5} \text{m}$. The R^2 error of the linear fitting equation is 0.90.

Figure 5b shows the comparison between the Kurz and Fisher model in Eq. (3), the linear fit in Eq. (4), and the experimental data. The major difference between the Kurz and Fisher model and the linear fit is that the linear model has an offset at the origin while the Kurz and Fisher model does not. The deviation of the Kurz and Fisher model might be a result of the rapid cooling rate and complex geometry of the dendrite tips instead of the simple assumptions of the model 1,34,57,58; it may also be caused by uncertainty in the measurement of the dendrite arm spacing.

Relationship between thermal history and mechanical properties

Figure 6a shows the correlation between thermal history and UTS for all locations on three cases (Cases A, B, and C). Three repeated experiments are conducted for each case. Each point on the plot represents the cumulative time spent in a given temperature range for a particular simulated temperature history; the color of each point represents the experimentally measured UTS for the corresponding location, while the symbol shape (circle, triangle, or star) denotes the three different walls (Case A, B, and C). Details of calculating the cumulative time of thermal histories in each temperature band are described in Methods and Supplementary Fig. 4. Case C (the 120 mm wall with 5 s dwell time) shows higher UTS than the walls without dwell time. It is conjectured that



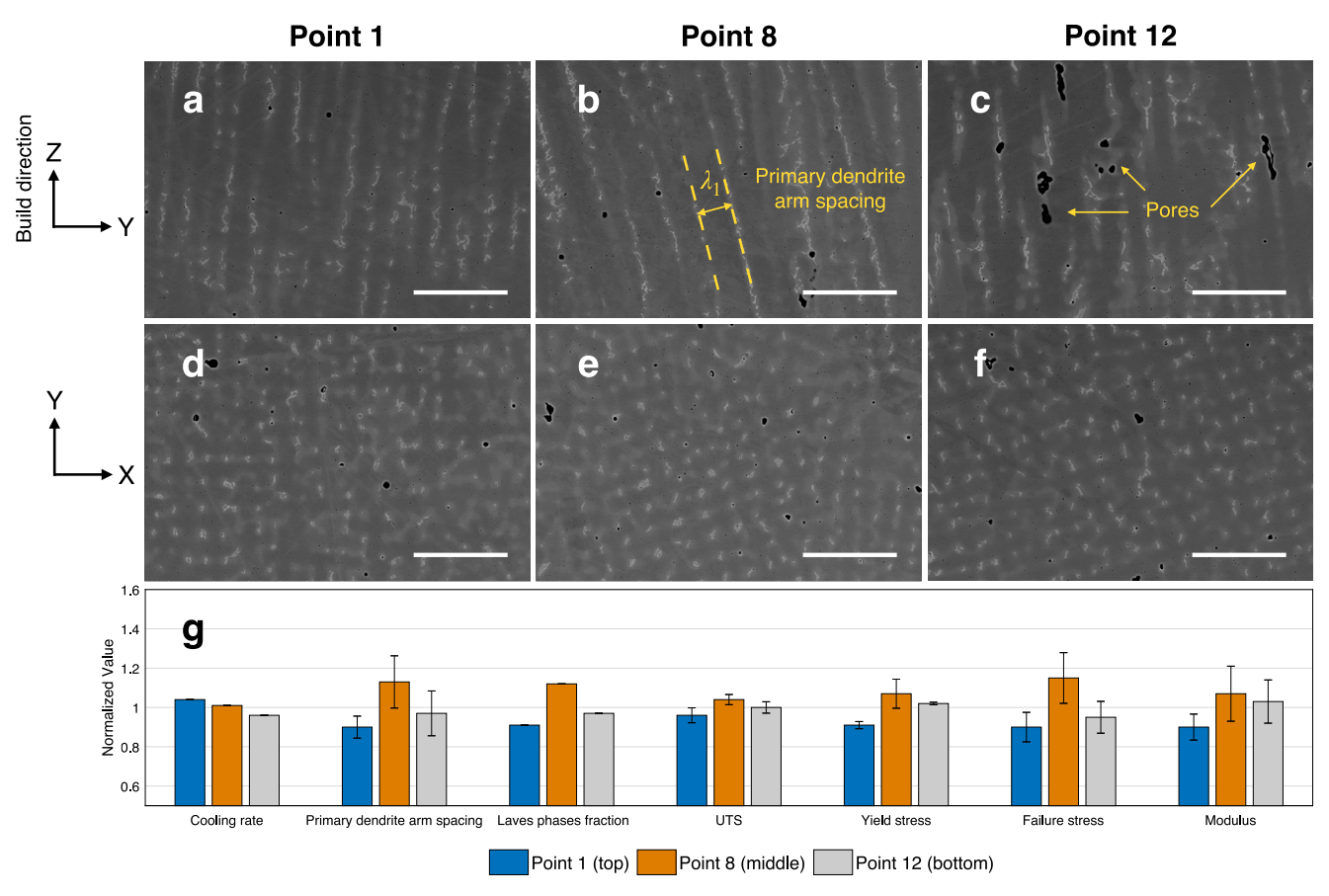


Fig. 4 SEM microstructure images for different locations in Case B. High magnification images a, b, and c are side views (normal to the scan direction) of the three locations noted in Supplementary Fig. 3. Images d, e, and f show top views (normal to the build direction) of the same locations. g Comparison of computed cooling rate, microstructure, and mechanical properties of different locations in the wall for Case B. Values are tabulated in Supplementary Table 6, normalized by the mean across the three locations. The error bars for primary dendrite arm spacing, UTS, yield stress, failure stress, and modulus give standard deviations of repeated experiments. Cooling rate and volume fractions of Laves phases are calculated based on a single simulation and measurement and therefore have no standard deviation reported. The scale bars in (a-f) are 50 µm.

increasing dwell time during deposition leads to an increased cooling rate (refer to Fig. 3g), resulting in finer microstructure and higher strength.

For the temperature between 1200 and 1533 K in Fig. 6a, less time is spent during each temperature band for Case C (with dwell time) than Case B (the same wall size without dwell time), which also indicates faster solidification in Case C. For temperatures below 1200 K, much more time is spent in each temperature range in Case C. Both shorter time spent during solidification and longer time spent at more moderate temperatures correlate with higher UTS. Likewise, Case B samples have higher UTS than Case A in Fig. 6a, and comparatively more time is spent in each temperature range for Case B. This is caused by the longer wall length and scan path in Case B, giving longer times between successive laser passes.

The zone enclosed in a red dashed line in Fig. 6a represents the portion of the thermal history after the laser is turned off. For the laser-off region, time spent is approximately the same for the three walls, indicating that differences in temperature history after laser shut-off do not play a role in the differences in mechanical properties in our tests.

Similar correlation maps with point colors corresponding to yield stress, failure stress, and elastic modulus are shown in Fig. 6b–d. Trends in yield and failure stress are similar to those of UTS. However, there is no apparent difference in modulus among the walls. This indicates that different microstructures caused by

thermal history features may lead to variations in material strength, but minor effects on elastic modulus.

Figure 6e is the relationship between the cooling rate and UTS for three different thin walls. The green line in Fig. 6e is the linear fit to all data. The R^2 error for the fit is 0.32. Results show that UTS increases as the cooling rate increases. Case C has the largest UTS with the largest cooling rate among the three cases. But the correlation between cooling rate and UTS for each case is weak, indicating that cooling rate by itself is not enough to predict mechanical properties. We need to consider more factors or features in the thermal histories besides cooling rate to predict mechanical properties.

Prediction of mechanical properties using 1D CNN

In the previous section, we discuss the trends in mechanical properties with respect to observable features of the temperature history, such as cooling rate and the reduced-order temperature feature descriptors (time spent during each temperature interval). However, the cooling rate alone is insufficient in predicting mechanical properties, and it is difficult to express a quantitative relationship between properties and the reduced-order temperature descriptors we highlight. Therefore, we aim to use machine learning to extract important features of the thermal histories and construct predictive models of the properties from a given thermal history.

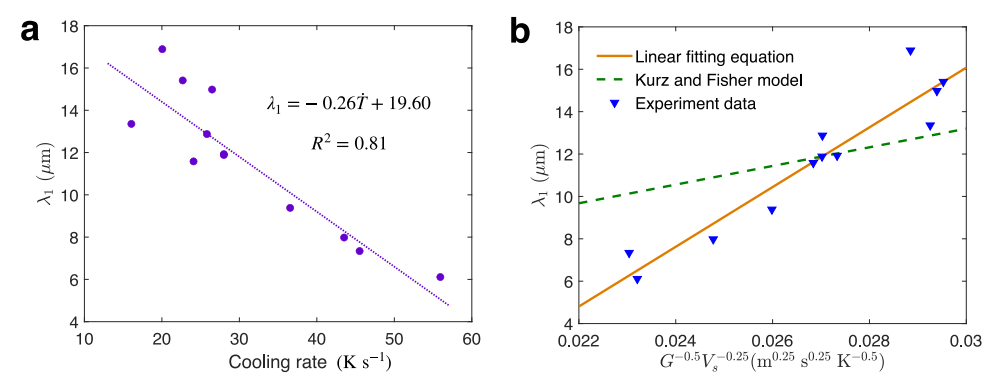


Fig. 5 Analysis of the primary dendrite arm spacing. a Primary dendrite arm spacing vs cooling rate. The dotted line is the linear fit, $\lambda_1 = -0.26\dot{T} + 19.60$, where λ_1 is the primary dendrite arm spacing (μ m) and \dot{T} is the cooling rate (K s⁻¹). The R^2 error for the fit is 0.81. Detail values and locations of samples are tabulated in Supplementary Table 7. **b** Comparison of measured primary dendrite arm spacing with analytical models. The solid line is the best fit to a model linear in $G^{-0.5}V_s^{-0.25}$ in Eq. (4), while the dashed line is the analytical model of Kurz and Fisher in Eq. (3). The R^2 error for the linear fitting equation is 0.90. The R^2 error for the Kurz and Fisher model is 0.47.

A convolutional neural network (CNN) can automatically extract essential features and can learn high-level features from spatial and temporal data^{36–39}. Recent work shows that one-dimensional CNN can be used to analyze time series or sequence data effectively^{40–45}. This work uses 1D CNN to extract features from thermal histories and predict mechanical properties, such as UTS, yield stress, failure stress, and modulus of the sample points. The data preparation, hyperparameter search, and neural network architecture are discussed in "Methods".

Figure 7 is the convolutional neural network structure with the intermediate convolutional layer visualization. The input of the trained CNN is the temperature history for each probed location in the deposited thin wall. The output of the network is UTS for corresponding locations. Figure 8 shows the comparison of CNN-predicted UTS with the actual measured UTS. Figure 8a is the training data while Fig. 8b is the test data. The R^2 scores for the training and testing are 0.96 and 0.67, as shown in the plot. The results show that the proposed CNN structure can accurately predict the UTS for samples in these thin-wall builds based on thermal history.

In a similar way, we also use the 1D CNN to predict other mechanical properties including yield stress, failure stress, and modulus. The prediction results based on training and testing data for yield stress, failure stress, and elastic modulus are shown in Supplementary Figs. 5–7. The R^2 scores for predicting yield stress, failure stress, and modulus for the training data are 0.82, 0.72, and 0.37, respectively; for test data, they are 0.70, 0.60, and 0.14. These results show that the proposed CNNs can also predict yield stress and failure stress with good accuracy. The prediction for modulus using the CNNs is not good, which is expected, because modulus is mainly a function of material type, and not highly correlated with the microstructural differences that depend on thermal history 59,60 . We can also see there is no strong correlation between thermal histories and modulus in Fig. 6d.

To understand which features of the thermal processes have a dominant effect on mechanical properties, we output the intermediate convolutional layers of the trained network. We visualize the output of the first, second, and third convolutional layer (Conv1D_1, Conv1D_2, Conv1D_3) for all feature filters; these are displayed above the CNN model in Fig. 7 and enlarged views are shown in Fig. 9. The channel outputs of each convolution layer inform how the convolutional layers extract the key factors from the temperature history and transfer useful information to formulate the mechanical properties. There are 32, 64 and 64 channels in the Conv1D_1, Conv1D_2, and Conv1D_3 layers, respectively.

Figure 9 shows the output from the first, second, and third convolutional layer for all feature filters or channels. Figure 9a is the output of the first convolutional layer for all channels. There are 32 feature filters for the Conv1D_1. The non-zero output plots display two main patterns. One pattern, displayed for example by the first feature filter, has the most values in the top few time steps. The other pattern has values from 0 s to around 1100 s, as seen for example in the third feature filter. Some other outputs in Fig. 9a are not activated and close to zero, which means that these feature filters do not capture trends from the input and do not transfer any information to the next layer in the network. A comparison of the extracted features output for the first and third feature filters of the Conv1D_1 with temperature history is shown in Fig. 9b and c, respectively. The blue line represents the temperature history. The red dot line represents the extracted output of the first convolutional layer for the first and third feature filters. The original extracted feature values are multiplied by 8000 for convenient comparison with temperature history in the same plot. The results indicate not only the temperature during the first few cycles (the solidification range) influence mechanical properties, but also the entire temperature history from the start of the laser scan to the end of the process (around 1100 s) plays an important role. The cooling rate calculated from the solidification period cannot represent all thermal features on the effect of mechanical properties. Both the solidification temperature and whole repeated thermal cycle during laser scan affect the formation of microstructure and final mechanical properties, such as UTS.

We also show the output of the second and third convolutional layers in Fig. 9d and e. There are 64 feature filters for Conv1D_2 and Conv1D_3. Comparing the outputs from the Conv1D_1, Conv1D_2, and Conv1D_3, the Conv1D_1 captures most of the information from the input, although some feature filters are not activated. For deeper layers, the output visualization becomes more abstract and less interpretable. The Conv1D_3 contains less information in the output visualization, with mostly zero output for a number of feature filters.

The comparison of the extracted features of the Conv1D_3 for one chosen feature filter with temperature history is presented in Fig. 9f, and all feature filters are shown in Fig. 9g. In Fig. 9f, the extracted features capture the temperature information from 0 s to around 1150 s. Looking at extracted features from all feature filters in Conv1D_3 in Fig. 9g, the output captures temperature information from the start of the laser scan to the end of laser fusion, which is similar to the trend of the outputs from Conv1D_1 and Conv1D_2.



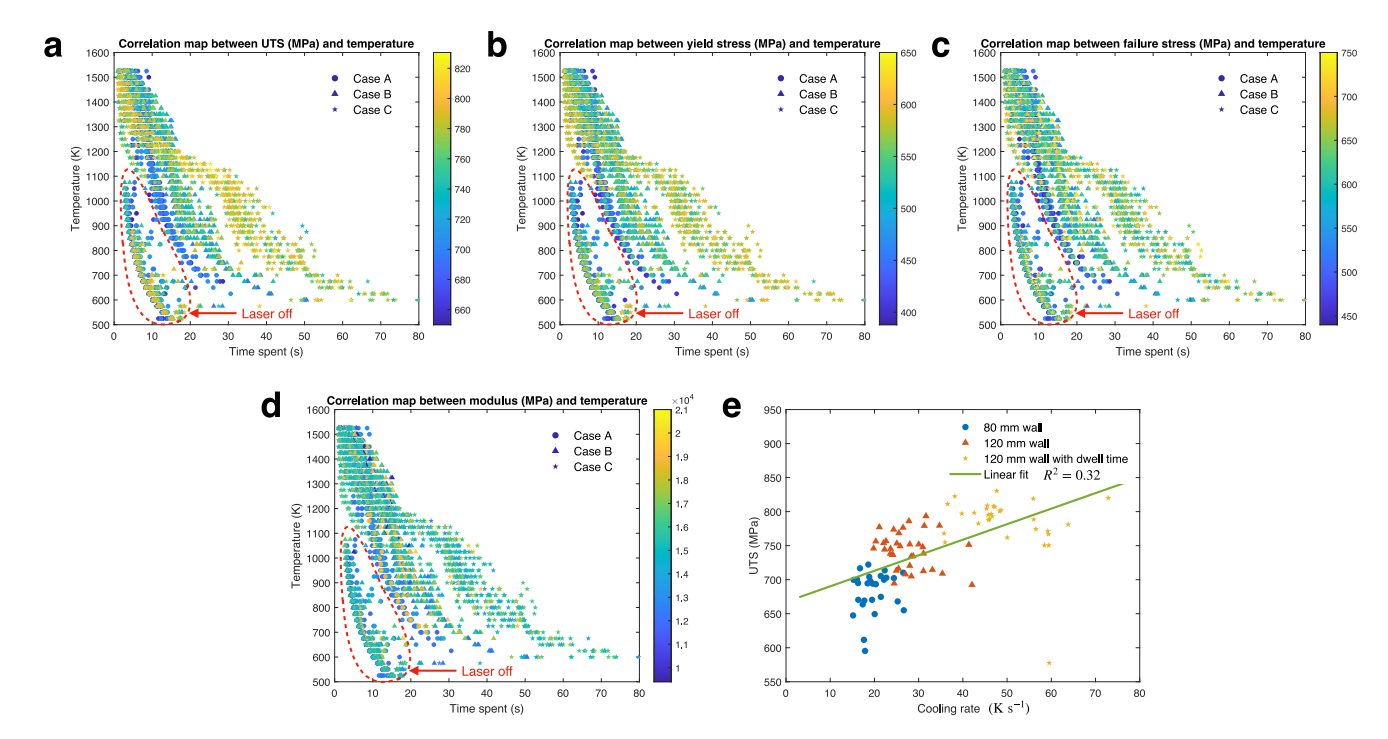


Fig. 6 Correlation between temperature and mechanical properties for three cases. a UTS b yield stress c failure stress d modulus. The location of each marker shows how much time was spent within each 25-degree temperature band. Details of temperature post processing is described in Methods and Supplementary Fig. 4. The color of each marker represents the value of the mechanical property for that sample. e Correlation between cooling rate and UTS for the three walls. The green line is the linear fit to all data. The R^2 error for the fit is 0.32.

It is often difficult to understand the relationship between inputs and outputs in a machine learning model like CNN, but in an attempt to further reveal the contribution of thermal histories to the UTS prediction, we compare the extracted features from the first convolutional layer (Conv1D_1) for multiple high and low UTS cases in Fig. 10. For ease of comparison, we selected 12 samples across all three wall cases that have similar total laser scanning time (from material deposition to laser-off time), and separated into high and low UTS groups (six samples in each group). The average UTS is 780.90 MPa and 695.93 MPa for the high and low UTS groups, respectively. Details of the samples in both groups are tabulated in Supplementary Tables 8 and 9. For both groups, the first and third features of the first convolutional layer are plotted in Fig. 10. Patterns are discerned for both features across the two groups. For the first feature (Fig. 10a and c), which is prominent over the first 300 s of cooling, the extracted signal is in general stronger for the high UTS group, with fewer non-zero values than for the low UTS group. For the third feature filter (Fig. 10b and d), low UTS cases (Fig. 10d) begin with a high signal but decrease over the first 200 s, after which they plateau at a value around 0.02-0.03 before decaying after laser-off time around 500 s. High UTS cases (Fig. 10b) maintain a higher signal between 0.04 and 0.06 until the laser-off time. Although we are not able to draw conclusions from these plots about what physical phenomena are involved, these results indicate that there may be two separate phenomena influencing UTS; one at early times and high temperatures (the first feature filter), and another at longer times and more moderate temperatures (the third feature filter).

DISCUSSION

In this work, we developed a validated finite element model with a data-driven CNN model to investigate the correlation between thermal history, microstructure, and mechanical properties during the DED process with Inconel 718. Instead of using experimental measured IR temperatures with uncertainties, we used simulated

temperature histories from a thermal model, validated by in situ experiments, to predict mechanical properties by CNNs. Simulated thermal histories, microstructures, and measured mechanical properties were thoroughly analyzed to understand the process-structure-property relationship. Key features from thermal histories were identified efficiently by the CNNs.

The results demonstrate the powerful ability of the 1D CNN model to predict mechanical properties, including UTS, yield stress, and failure stress using simulated, as opposed to measured, thermal histories. The 1D CNN model is effective and efficient in identifying important hidden features from complex thermal histories with good accuracy. The extracted features of thermal histories show different contributions for high and low UTS samples. For low UTS samples, early thermal cycles contribute most strongly to the filtered features, with relatively small contributions from later histories. High UTS samples show a stronger feature signal throughout the later times and more moderate temperatures. These results emphasize the importance of considering the entire thermal history rather than simple thermal metrics, such as cooling rate, for accurate predictions of mechanical properties. By using simulated temperatures instead of experiments, the data-driven CNN model extends the ability to predict and monitor mechanical properties for AM builds of complex part geometries.

The extracted features of the 1D CNN model can give insights into microstructure evolution. From visualization of intermediate convolutional layers, it is observed that not only the solidification range but also the entire thermal history during the laser scan has effects on final mechanical properties. This might indicate that some precipitates, such as Laves phases, δ phase (Ni₃Nb), γ' phase Ni₃(Al, Ti) and γ'' phase (Ni₃Nb), form during the intermediate temperature range. γ'' phase is the major strengthening precipitation in Inconel 718 alloy while γ' phase is an assistant strengthening precipitate⁵⁰. The δ phase and Laves phases are detrimental to material properties (strength, fatigue life, and ductility)⁶¹.

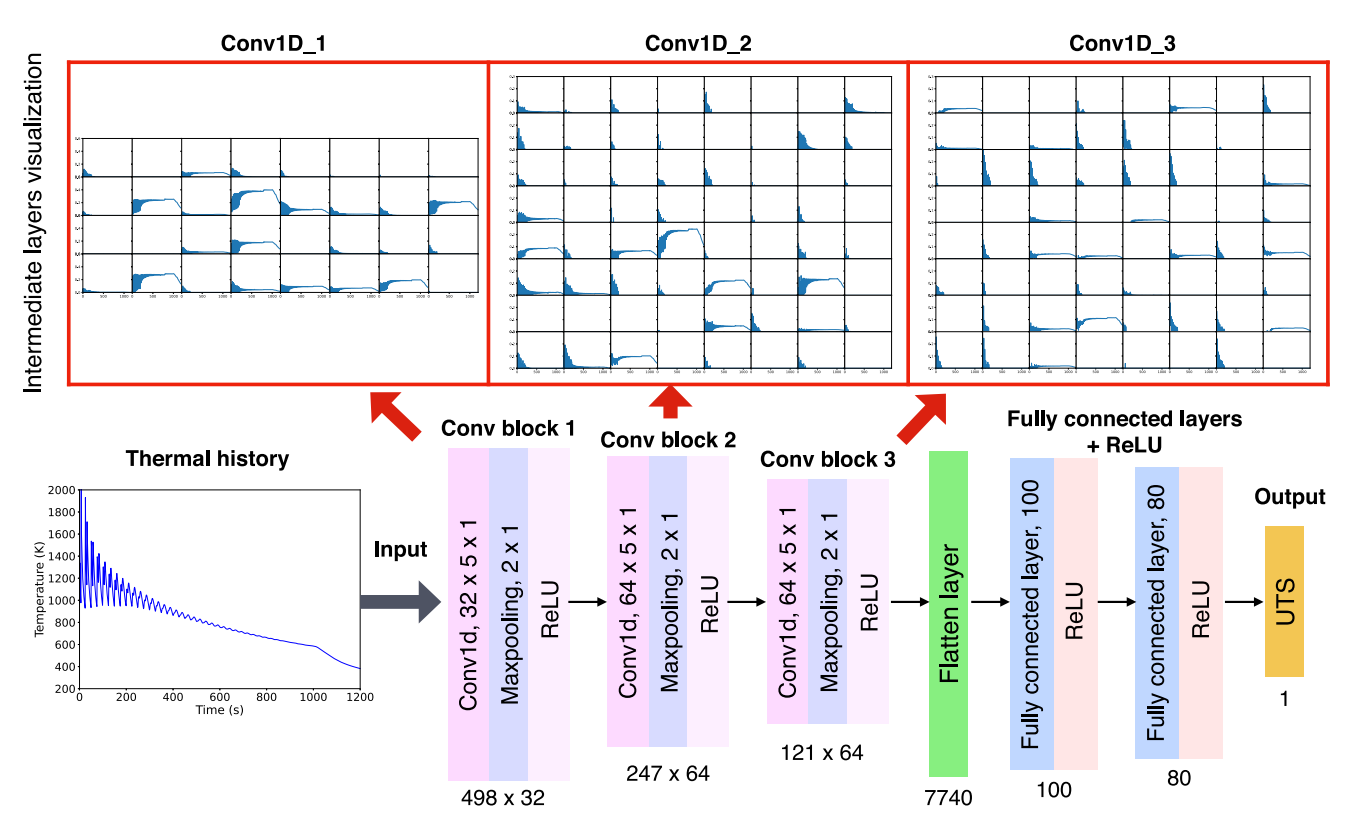
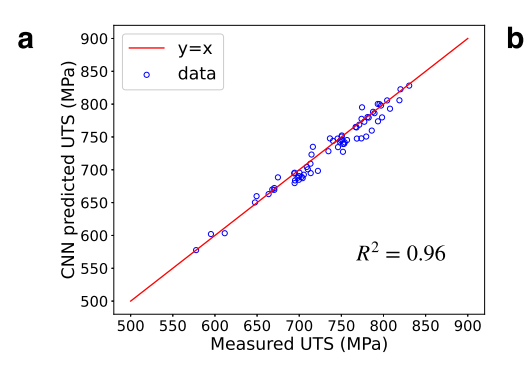


Fig. 7 The CNN structure with intermediate layer visualization. The CNN architecture consists of three convolutional layers with max pooling layer and the ReLU activation, and fully connected layers with the ReLU activation. The top three subplots are the visualization of output of the first, second, and third convolutional layers. The inputs of 1D CNN are the pre-processed thermal histories. The output is mechanical properties (UTS).

Different precipitates can form in two stages: non-equilibrium solidification and solid-state phase transformation after solidification. In non-equilibrium solidification, the y matrix begins to solidify when the temperature is below the liquidus temperature during the first several thermal cycles. The segregation of Inconel 718 component elements changes the driving force of phase formation, which leads to the formation of Laves phases in the interdendritic region⁶². It has been reported that Laves formation is related to slow solidification at a low cooling rate⁶³. However, it is not sufficient to use cooling rate alone as the criterion of Laves formation because Laves phases are also observed at high cooling rates in AM processes^{64,65}. Thermal gradients, undercooling and solid-liquid interface velocity should also be considered. As the temperature continues to drop after non-equilibrium solidification, solid-state phase transformation occurs. Precipitates such as δ , γ' and $y^{''}$ phases may form in this stage. If time is sufficient between deposition of layers (e.g., for long dwell time), temperature decreases quickly, and the time that material spends in the precipitation formation temperature range (875–1275 K) from the TTT (Temperature-Time-Transformation) diagram of Inconel 718^{50,66} is too short to form δ , γ' and γ''^{62} . If the dwell time is not long enough to cool the material guickly, time spent in the precipitation temperature range may be long enough to form δ , γ' and y'' in the microstructure. Note that the time required to form precipitates has been observed to be shorter for AM than for wrought Inconel 625 due to increased interdendritic segregation in AM material $^{67-69}$. In Inconel 718, the γ' phases and γ'' precipitation temperature range is from 875 to 1175 K, while that for δ phases is from 1225 to 1275 K^{61,70,71}. Both temperature ranges for precipitation are within the intermediate temperature range identified from the visualization of our CNN feature filters. Therefore, CNN predictions may give more insights for future models to predict the formation and evolution of precipitates and correlate with mechanical properties.

To maintain computational efficiency, the thermal model neglects fluid flow in the melt pool, along with other powderscale details during deposition. Because of these assumptions, complex flow features and heat transfer mechanisms during powder deposition in the melt pool are not captured. For powder bed processes, it has been shown that ignoring convection in the melt pool results in less heat dissipation throughout the melt pool, overestimation of the melt pool width, and higher peak temperature^{72,73}. High-fidelity models, such as thermal-fluid models, can capture more physics details and provide more accurate predictions than the conduction-only thermal model. However, because of the computational expense of thermal-fluid models, including fine grid and time step size requirements, they are limited to small volumes, and repeated part-scale simulations are infeasible. On the other hand, we expect the most important portion of the thermal history to occur during and after final solidification at each material point; this history is expected to be less impacted by the neglect of flow in the melt pool just after powder deposition at each point. The validation of our simulations in the section "Thermal simulation and validation" demonstrates the accuracy of the simulations for the desired temperature regime. Although it lacks the fidelity of more computationally expensive models, the form of thermal model we choose provides an efficient approximation of the true thermal history that we find can be reliably used, through our data-driven model, to predict resulting material properties. To further improve the accuracy of temperature predictions, rather than increasing model fidelity, it is important to better characterize boundary conditions and surface parameters. For example, the convective heat transfer at all surfaces and the temperature-dependent radiative emissivity of





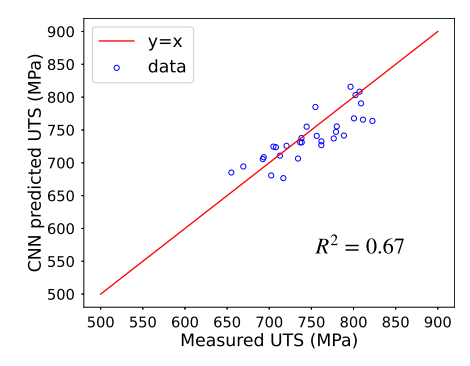


Fig. 8 Measured UTS versus predicted UTS. a Training data. b Test data.

the material have an impact on the computed thermal histories; the emissivity also affects the interpretation of IR camera data used for calibration and validation of the simulations.

With enough microstructural data for training, the CNN could in principle be extended to predict microstructure information such as primary dendrite arm spacing based on thermal histories. However, dendrite spacing is measured from the SEM characterization images of experimental samples, which is expensive and time-consuming, and sufficient data is unavailable. We also observed defects, including pores, in SEM images. Pore formation is expected to be highly related to thermal history and can affect mechanical properties, as demonstrated in our prior work⁵². Further study could incorporate the porosity information into the data-driven model to investigate this process-structure-properties relationship; currently, the effects of porosity are captured indirectly through the CNN relating temperature to properties.

The proposed data-driven CNN framework has great potential for predictions of mechanical properties for complex parts built with AM and provides physical insights on thermal effects on microstructure and mechanical properties. Our findings indicate that the entire temperature-time history, which can be approximated through validated thermal simulation, influences mechanical properties. This approach and the insights gained through it can provide valuable information in the design and improvement of DED and other AM processes.

METHODS

DED experiment setup and material

Single-track thin walls of Inconel 718 were deposited via DED onto stainless steel 304 substrates using a hybrid additive and subtractive DMG MORI Lasertec 65 machine equipped with an in situ infrared melt pool monitor. The walls were produced using three different process conditions to vary the solidification and cooling rates between different cases: 80 mm long walls (Case A), 120 mm long walls (Case B), and 120 mm long walls with a 5 s inter-layer dwell time (Case C). Three repeated experiments are conducted for each case. Each wall is built with 120 layers. The laser power is 1800 W, and the laser scan speed is 16.7 mm s⁻¹ for all builds. The design of the laser tool path in the experiment is shown in Supplementary Fig. 1b. The powder mass flow rate is 0.3 g s⁻¹ with a powder focus radius of 3 mm. For Case C, after the deposition of each layer, a 5 s dwell time (a pause in the build) is applied before beginning the next layer, allowing for additional cooling.

IR thermal measurement and calibration

In the deposition process, a FLIR A655sc digital IR camera was used to capture thermal images of the thin wall during deposition. The resolution of the camera is 640×480 pixels, and the spectral range is from 7.5 to 14.0 µm with an accuracy of ± 2 °C. The IR camera recorded the infrared radiation during the process; temperature measurements were then obtained from the raw IR radiation data by calibrating the emissivity at the measured points. The signals from IR cameras are related to material emissivity, surface condition, and detector efficiency. In order to accurately convert emission temperature to absolute temperature, the emissivity of

the material must be determined. The emission temperature is calibrated using the discontinuities observed at the start and end of the liquidus-solidus transition region. Additional details of emissivity calibration are given in ref. ²².

Mechanical properties measurement

Coupon specimens were cut via wire EDM for each wall, and measurements were performed for modulus, UTS, yield stress, yield strain, failure stress, and failure strain. The miniaturized ASTM E8 tensile specimens were cut with test direction in the build (z) direction and were manufactured from 9 different locations on each 80 mm wall (Case A) and 12 different locations on each 120 mm wall (Cases B and C). The temperature monitored by the IR camera and the locations of coupon specimens for tensile tests are shown in Supplementary Fig. 1 for reference; Supplementary Fig. 1d shows locations of coupon specimens in Case A, while Supplementary Figure 1e shows the locations of specimens in Cases B and C. The sizes of tensile test specimens are shown in Supplementary Fig. 8. The nominal dimensions of the gage section are 0.8 mm thick by 1.2 mm wide by 2.5 mm long. The tensile tests were conducted under displacement control until fracture with a pull rate of 0.02 mm s⁻¹ on a Sintech 20 G tensile test machine. More details of tensile tests and coupon dimensions can be found in ref. ⁷⁴. A typical stress-strain curve for one sample of Case A is provided in Supplementary Fig. 9 for reference. The yield stress, failure stress, UTS, and Young's modulus are measured from the stress-strain curve.

Microstructure characterization

Subsets of the tensile specimens from selected wall locations were cut, mounted, and polished to a 0.02 µm finish with non-crystallizing colloidal silica on a vibratory polisher. Microstructures at two faces of samples were observed, normal to the build direction and the scan direction, with a FEI Quanta 650 scanning electron microscope (SEM) with secondary electron (SE), backscatter electron (BSE), and energy-dispersive x-ray spectroscopy (EDS) detectors. Binarization and analysis of the SEM images were performed by ImageJ Software⁵¹.

Thermal model

The thin-wall builds are simulated using a finite element model. The thermal history during the DED process is calculated by solving the heat conduction equation in the following form:

$$\rho C_{p} \frac{\partial T}{\partial t}(\mathbf{x}, t) = -\nabla \cdot \mathbf{q}(\mathbf{x}, t) \tag{5}$$

where ρ is the material density, C_{ρ} is the specific heat capacity, T is temperature, t is time, \mathbf{q} is heat flux, and \mathbf{x} is the spatial coordinate.

The heat flux vector in Eq. (5) is assumed to be given by Fourier's law:

$$\mathbf{q} = -k\nabla T \tag{6}$$

where k is the thermal conductivity of the material, modeled as isotropic (so that k is a scalar). The thermal properties of Inconel 718, namely the specific heat capacity and thermal conductivity, are taken as temperature-dependent with values listed in Supplementary Table 10. Properties at temperatures between those in the table are calculated by linear interpolation.

The thermal model does not consider fluid flow in the melt pool, or any resulting convection or surface motion. Surface tension, Marangoni forces,

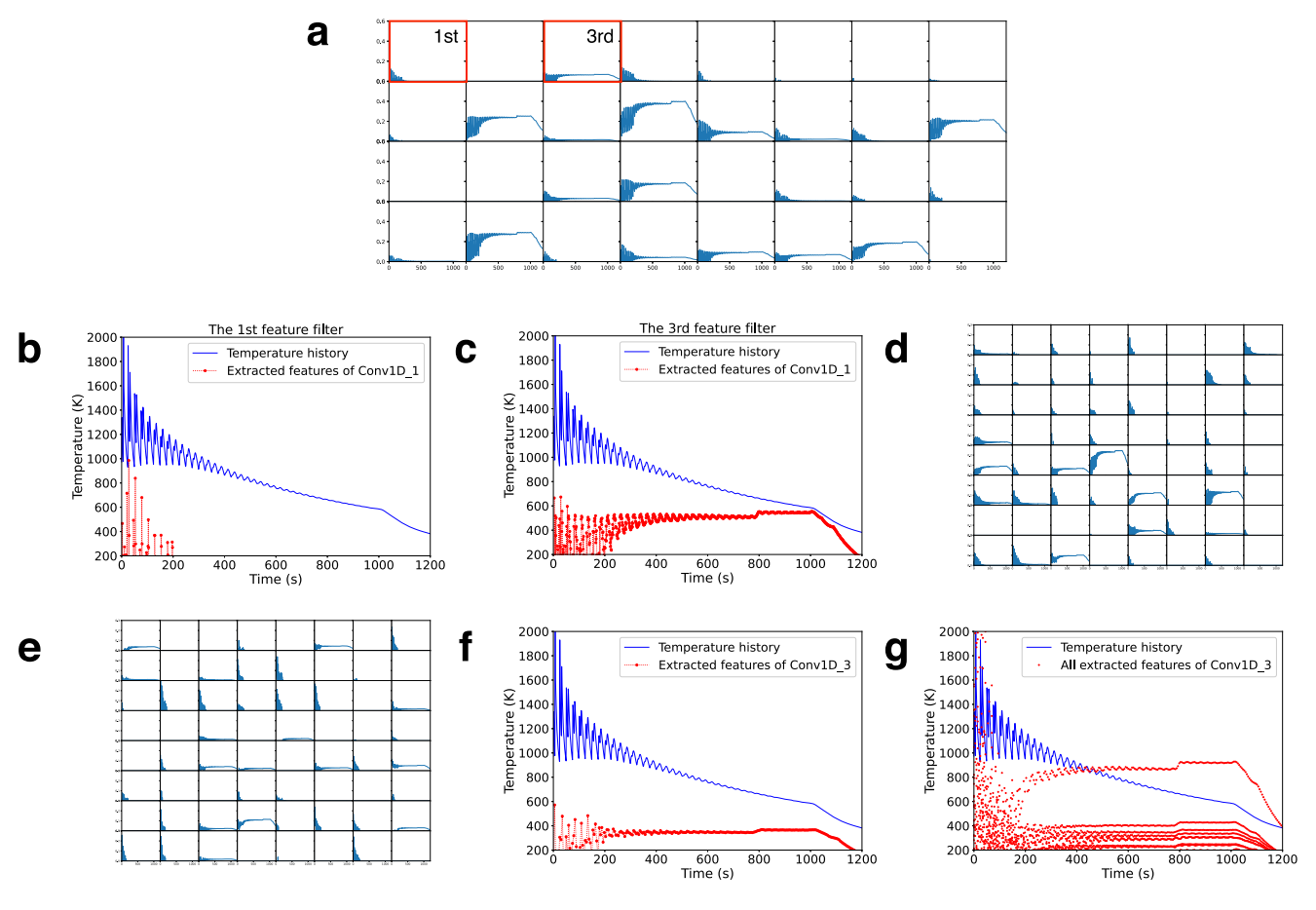


Fig. 9 The output of the first, second, and third convolutional layer (Conv1D_1, Conv1D_2, Conv1D_3) for all channels. a Conv1D_1. d Conv1D_2. e Conv1D_3. Each subplot in a, d and e represents the output of the layer for a single one of the 32, 64 and 64 channels or filters. b, c Comparison of temperature history with extracted features from the Conv1D_1 with the first and third feature filter. f, g Comparison of temperature history with extracted features from the Conv1D_3 for f a single feature filter and g all feature filters. The blue line represents temperature history of one case. The red dots are the extracted features from feature filters in the convolutional layer. The original extracted feature values are multiplied by 8000 for convenient comparison with temperature history in the same plot.

buoyancy, viscosity, and recoil pressure due to evaporation are thus all neglected. The model also ignores chemical element diffusion, chemical reaction, material composition change, and microsegregation of solutes during solidification.

Initial and boundary conditions

The initial condition for the thin wall deposition and substrate is a constant temperature:

$$T(\mathbf{x}, t_0) = T_{\infty} \tag{7}$$

where T_{∞} is the ambient air temperature. The boundary condition describes the heat flux at the surface of the domain, which includes the heat loss due to radiation, convection, evaporation, and heat source from laser. The general form of the heat flux boundary condition is

$$\mathbf{q} \cdot \mathbf{n} = q_{\text{rad}} + q_{\text{conv}} + q_{\text{evap}} + q_{\text{laser}} \qquad \text{on } \Gamma_q$$
 (8)

where Γ_q is the boundary surface with normal vector \mathbf{n} , $q_{\rm rad}$ represents the radiative heat flux applied on all exposed surfaces of the thin wall and substrates, $q_{\rm conv}$ is the heat flux due to convection on all surfaces (free convection with constant coefficient on the bottom of the substrate, and forced convection with spatially varying coefficient on the surface of the walls and other surfaces of substrate), $q_{\rm evap}$ is the heat flux due to evaporation, and $q_{\rm laser}$ is the laser heat flux that is applied on the exposed surfaces of the thin wall and the top surface of the substrate. Note that the exposed surfaces change throughout the build process as the material is added. During the simulated build, elements representing newly added material are activated on a schedule determined by the laser path. Only active elements are

considered in the computation, and the above boundary condition is applied at the outer boundary of the active domain at each time step.

The heat flux boundary condition due to radiation exchange with the ambient surroundings is applied on all exposed surfaces of the thin wall and substrate:

$$q_{\rm rad} = \varepsilon \sigma (T^4 - T_{\infty}^4) \tag{9}$$

where ε is the material emissivity and σ is the Stefan-Boltzmann constant. The heat flux due to convection is

$$q_{\text{conv}} = h(x, y, z)(T - T_{\infty}) \tag{10}$$

where h is the heat convection coefficient, x, y, and z are the coordinates of the point of interest. At the bottom surface of the substrate, constant free convection is applied with a convection coefficient of $10 \, \text{W m}^{-2} \, \text{K}^{-1}$ to approximate free convection in air^{13,75–78}. At the exposed surfaces of thin wall and the top surfaces of the substrate, we use the same form of spatially varied heat convection coefficient model as ref. ³. The spatially varying convection model presented in ref. ³ accounts for the effects of forced convection caused by the shield and carrier gas flows in the DED process. The heat convection coefficient on the wall surfaces is in the form:

$$h_{\text{wall}}(x,y,z) = \begin{cases} (-2.0\Delta z + 15)e^{-\left(0.107\sqrt{(x-x_b)^2 + (y-y_b)^2 + (z-z_b)^2}\right)^{2.7}} + 10 & \Delta z \le 7.0 \,\text{mm} \\ 10 & \Delta z > 7.0 \,\text{mm} \end{cases}$$
(11)

where Δz is the vertical distance from the top surface of the wall to the point of interest, x, y, and z are the coordinates of the point of



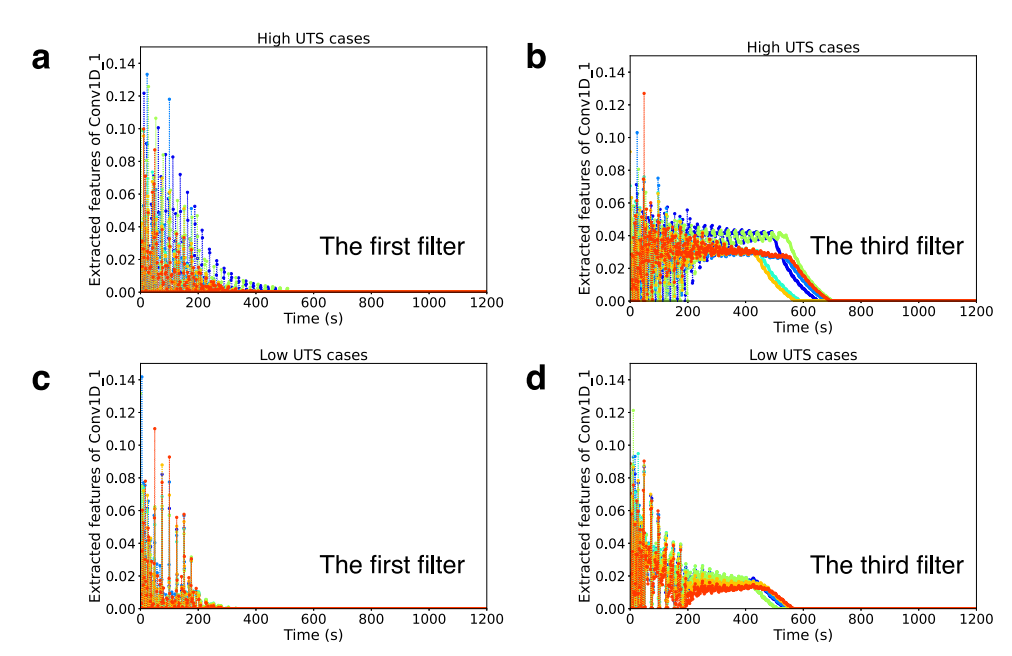


Fig. 10 Comparison of extracted features of the first convolutional layer (Conv1D_1) for high and low UTS cases. a, c Extracted features of Conv1D_1 with the first feature filter for high and low UTS cases. b, d Extracted features of Conv1D_1 with the third feature filter for high and low UTS cases.

interest, and x_b , y_b , and z_b are the coordinates of the center of the laser beam

Since convection on the vertical surfaces of the thin wall is expected to be different from that on the horizontal substrate surfaces, a slightly different model is applied to the substrate³. We also use the same form of the equation as ref. ³ for the convection on the top surface of the substrate stated below:

$$h_{\text{substrate}}(x,y,z) = \begin{cases} 1.9(-2.0\Delta z + 15)e^{-(0.031\sqrt{(x-x_b)^2 + (y-y_b)^2 + (z-z_b)^2})^{1.4}} + 10 & \Delta z \leq 7.0 \text{ mm} \\ 10 & \Delta z > 7.0 \text{ mm} \end{cases}$$
(12)

The parameters in both of these expressions for convection coefficient are calibrated using the DED experiment data.

The heat loss due to evaporative cooling when the material reaches the evaporation temperature is

$$q_{\rm evap} = -m_{\rm evap} L_{\rm v} \tag{13}$$

where m_{evap} is the mass evaporation flux and L_{v} is the latent heat of vaporization. The mass evaporation flux term in Eq. (13) follows the model proposed by Anisimov⁷⁹:

$$m_{\text{evap}} = P_{\text{sat}}(T) \left(\frac{m_{\text{mol}}}{2\pi R_{\text{nas}} T} \right) \tag{14}$$

where $P_{\rm sat}$ is the saturation pressure at temperature T, $R_{\rm gas}$ is the gas constant, and $m_{\rm mol}$ is the molar mass of the evaporating species. Specifically, the saturation pressure $P_{\rm sat}$ can be computed by solving the Clausius-Clapeyron equation⁷⁹:

$$P_{\text{sat}}(T) = P_{\text{a}} \exp\left(\frac{-L_{\text{v}} m_{\text{mol}}}{R_{\text{gas}}} \left(\frac{1}{T} - \frac{1}{T_{\text{b}}}\right)\right) \tag{15}$$

where T_b is the boiling point or the evaporation temperature at the ambient pressure P_a .

The laser heat flux boundary condition is applied on the exposed surfaces of the thin wall and the top surface of the substrate. The distribution of laser heat source is assumed to follow a Gaussian relationship in the following form:

$$q_{\text{laser}} = \frac{2\eta P}{\pi r_b^2} \exp\left(\frac{-2\left((x - x_b)^2 + (y - y_b)^2 + (z - z_b)^2\right)}{r_b^2}\right)$$
(16)

where η is the laser absorption efficiency, P is the laser powder, and r_b is the beam radius.

Simulation cases and integration method

The geometry of the computational domain and meshes are shown in Supplementary Fig. 1c. The dimensions of the thin walls are listed in Supplementary Table 1. The dimension of the substrate in each case is 200 mm \times 75 mm \times 75 mm in the x, y, and z direction. For each case, there are 120 deposition layers with a layer thickness of 0.5 mm. The laser power is $1800 \, \text{W}$ with the laser scan speed of $16.7 \, \text{mm s}^{-1}$. For Case A, the mesh contains 174,805 elements with 222,304 nodes; for Cases B and C, 238,613 elements with 300,036 nodes. For each layer, the mesh is discretized to contain one element in the building direction and six elements through the width of the wall. One element per layer for thin wall build mesh is found to be enough for computational accuracy since the depth of the melt pool is deeper than a single layer in the DED process. The time step size is 0.12 s for all cases. An element activation method is used to accommodate material addition during the DED process. The entire mesh is stored from the beginning of the simulation, but elements representing as-vet unbuilt material are inactive and not included in the finite element matrix assembly. Elements are activated according to the laser path and build schedule; as new elements are activated, the exposed surface on which boundary conditions are applied is also modified. More details of the computational approach can be found in ref. 52. An eight-point Gaussian quadrature scheme (two points in each direction) is used to evaluate spatial integrals in the finite element weak form. A backward Euler method is used to discretize the temporal term in Eq. (5). The Newton-Raphson method is used to solve the resulting equation set, which is nonlinear because of the radiation terms in Eq. (9).

Thermal history post-processing and cooling/solidification rates

During the AM process, the variation of mechanical properties is significant due to different thermal histories. To study the correlation between cooling time and mechanical properties (e.g., Fig. 6a–d), we extract a reduced set of data features from each thermal history by dividing each thermal history into different temperature ranges with 25 K intervals and then calculating the cumulative time spent in each temperature range after solidification (see Supplementary Fig. 4). Since we mainly focus on the thermal effects on mechanical properties during the material solidification period, we only consider the temperature history after the temperature decreases below the solidus temperature for the final time (the thermal history in the white area in Supplementary Fig. 4).

It is expected that the cooling rate affects the formation of microstructure and final mechanical properties^{21,80,81}. In this work, we

calculate the cooling rate as the average slope of the temperature history between the last crossing of the solidus temperature (1533 K) and an arbitrarily chosen temperature of 1450 K for all probed points. We calculated the cooling rate just after the last thermal cycle through the temperature range of 1533–1450 K, because it is expected that the last solidification event at a point will be most important in the resulting microstructure. An example of the cooling rate calculation is shown in Supplementary Fig. 10.

Since the primary dendrite arm spacing is related to the solidification rate and thermal gradient, we calculated the solidification rate from the simulated temperature fields as shown in Supplementary Fig. 11. The solidification rate is in the direction of the normal vector to the surface of the liquid-solid interface, which is divided by the red and orange colors. The solidification rate V_s can be calculated by $V_s = V \cos \theta$, where V is laser scan speed, and θ is the angle between laser scan direction and the direction of the normal vector to the liquid-solid interface. Since each point in the thin wall undergoes repeated thermal cycles, we only focus on process-structure properties during the solidification period and calculate the solidification rate at the last solidus temperature for the location.

Convolutional neural network

We use the 1D CNN to extract features from thermal histories and predict mechanical properties, including UTS, yield stress, failure stress, and modulus. The input of the CNN model is the thermal history at a given location in the form of a series of temperature values at regularly spaced points in time. The output is mechanical properties for corresponding locations. Since the IR-measured temperature does not capture the temperature through the important initial solidification range accurately, as shown in Fig. 2, we use simulated thermal histories instead of experimental data as input in the model. To prepare the thermal history curve at each sample point, we define the initial time t=0 as the time when the laser spot first reaches that location for each temperature history, i.e., when the material is first added at that location. Note that it is convenient to load each set of input data with the same size in the CNN. We pad the data to a uniform maximum time using a linear extrapolation down to the final constant ambient temperature, as shown in Supplementary Fig. 12. To reduce the computational cost, we sample every 10th point from the original data so that points are separated by a time interval of $\Delta t = 1.2$ s. We find that 1000 points provide enough resolution to define the temperature history curve accurately.

The CNN architecture used in this paper starts with three convolutional blocks as shown in Fig. 7. For each convolutional block, 32, 64, and 64 filters with 5×1 kernel size is chosen for the first, second, and third convolutional layer. Max-pooling layer with filter size of 2 × 1 is applied in each convolutional block, and a rectified linear unit (ReLU) activation is used for all convolutional and fully connected layers. The extracted information from previous convolutional blocks are flattened and fed to two fully connected layers with 100 and 80 neurons, respectively. The input data size is 1000, which is the length of the series of temperature values in time. The output size is 1. Both the input and output data are min-max normalized before loading into the CNN training. The Adam optimizer is used in training to minimize the mean squared error (MSE). An early stopping method is applied to prevent overfitting. The patience of the early stopping is 100 epochs, which means that the training will stop if the validation loss does not improve after 100 epochs. The data set is split into 70% for training and 30% for testing, and the test data is used to measure validation loss.

The MSE is defined in the following format:

$$MSE = \frac{1}{n} \sum_{i=1}^{n} (y_i - \hat{y}_i)^2$$
 (17)

To evaluate the performance of the CNN structure, the R^2 score is calculated based on the difference between predicted and measured UTS:

$$R^{2} = 1 - \frac{\sum_{i=1}^{n} (y_{i} - \hat{y}_{i})^{2}}{\sum_{i=1}^{n} (y_{i} - \bar{y})^{2}}$$
(18)

where \hat{y}_i is the predicted value of the *i*th sample, y_i is the actual value of the sample, \overline{y} is the mean of all actual data and n is the number of samples. The larger the R^2 , the better the prediction.

In this work, a grid search is applied to tune the hyperparameters in the CNN. A CNN consists of convolutional layers, pooling layers, and fully connected layers. In the convolutional layer, the hyperparameters include the number of filters, kernel size, and stride numbers. For the pooling layer,

the hyperparameters include the filter size, padding, and stride numbers. We also need to decide the number of convolutional blocks, the number of fully connected layers, and the number of neurons per layer. For hyperparameter tuning, we search for the number of convolutional blocks and filter size with a pre-chosen kernel size of five and a stride size of one. The number of convolutional blocks varies from two to five and the filter size varies from 32 to 256. We also search for the number of hidden layers in the fully connected layers and the number of neurons per layer, with hidden layer numbers varying from one to five, and the number of neurons varying from 10 to 100 with a step of 10. The performance of each CNN structure is evaluated based on the $\it R^2$ score.

DATA AVAILABILITY

The main data that support the findings of this study are presented in the paper and the Supplementary information. The datasets used in the CNN model are also provided at https://github.com/lichaofang/CNN_AM, including processed thermal histories and mechanical properties. Extra data are available from the corresponding author upon reasonable request.

CODE AVAILABILITY

The CNN Python code used in this study can be found in https://github.com/lichaofang/CNN_AM. Additional code used in this study is available from the corresponding author upon reasonable request.

Received: 16 September 2021; Accepted: 10 May 2022; Published online: 06 June 2022

REFERENCES

- Keller, T. et al. Application of finite element, phase-field, and CALPHAD-based methods to additive manufacturing of Ni-based superalloys. *Acta Mater.* 139, 244–253 (2017).
- DebRoy, T. et al. Additive manufacturing of metallic components-process, structure and properties. Prog. Mater. Sci. 92, 112–224 (2018).
- Heigel, J. C., Michaleris, P. & Reutzel, E. W. Thermo-mechanical model development and validation of directed energy deposition additive manufacturing of Ti-6Al-4V. Addit. Manuf. 5, 9-19 (2015).
- Wang, Z., Palmer, T. A. & Beese, A. M. Effect of processing parameters on microstructure and tensile properties of austenitic stainless steel 304L made by directed energy deposition additive manufacturing. *Acta Mater.* 110, 226–235 (2016)
- Gan, Z., Liu, H., Li, S., He, X. & Yu, G. Modeling of thermal behavior and mass transport in multi-layer laser additive manufacturing of Ni-based alloy on cast iron. Int. J. Heat Mass Transf. 111, 709–722 (2017).
- Wei, H., Mazumder, J. & DebRoy, T. Evolution of solidification texture during additive manufacturing. Sci. Rep. 5, 16446 (2015).
- Manvatkar, V., Gokhale, A., Reddy, G. J., Venkataramana, A. & De, A. Estimation of melt pool dimensions, thermal cycle, and hardness distribution in the laserengineered net shaping process of austenitic stainless steel. *Metall. Mater. Trans.* A 42, 4080–4087 (2011).
- Li, Y. & Gu, D. Parametric analysis of thermal behavior during selective laser melting additive manufacturing of aluminum alloy powder. *Mater. Des.* 63, 856–867 (2014).
- Foroozmehr, A., Badrossamay, M., Foroozmehr, E. & Golabi, S. Finite element simulation of selective laser melting process considering optical penetration depth of laser in powder bed. *Mater. Des.* 89, 255–263 (2016).
- Kelly, S. & Kampe, S. Microstructural evolution in laser-deposited multilayer Ti-6Al-4V builds: Part II. thermal modeling. *Metall. Mater. Trans. A* 35, 1869–1879 (2004).
- Labudovic, M., Hu, D. & Kovacevic, R. A three dimensional model for direct laser metal powder deposition and rapid prototyping. J. Mater. Sci. 38, 35–49 (2003).
- Jendrzejewski, R., Śliwiński, G., Krawczuk, M. & Ostachowicz, W. Temperature and stress fields induced during laser cladding. Comput. Struct. 82, 653–658 (2004).
- Wang, L., Felicelli, S. D. & Pratt, P. Residual stresses in LENS-deposited AISI 410 stainless steel plates. Mater. Sci. Eng.: A 496, 234–241 (2008).
- Ghosh, S. & Choi, J. Three-dimensional transient finite element analysis for residual stresses in the laser aided direct metal/material deposition process. J. Laser Appl. 17, 144–158 (2005).
- Tan, H. et al. Process mechanisms based on powder flow spatial distribution in direct metal deposition. J. Mater. Process. Technol. 254, 361–372 (2018).



- Chukkan, J. R., Vasudevan, M., Muthukumaran, S., Kumar, R. R. & Chandrasekhar, N. Simulation of laser butt welding of AISI 316L stainless steel sheet using various heat sources and experimental validation. J. Mater. Process. Technol. 219, 48–59 (2015)
- Denlinger, E. R., Jagdale, V., Srinivasan, G., El-Wardany, T. & Michaleris, P. Thermal modeling of Inconel 718 processed with powder bed fusion and experimental validation using in situ measurements. *Addit. Manuf.* 11, 7–15 (2016).
- Qian, L., Mei, J., Liang, J. & Wu, X. Influence of position and laser power on thermal history and microstructure of direct laser fabricated Ti–6Al–4V samples. *Mater. Sci. Technol.* 21, 597–605 (2005).
- Bai, X., Zhang, H. & Wang, G. Modeling of the moving induction heating used as secondary heat source in weld-based additive manufacturing. *Int. J. Adv. Manuf. Technol.* 77, 717–727 (2015).
- Bai, X., Zhang, H. & Wang, G. Improving prediction accuracy of thermal analysis for weld-based additive manufacturing by calibrating input parameters using IR imaging. Int. J. Adv. Manuf. Technol. 69, 1087–1095 (2013).
- Wolff, S. J. et al. Experimentally validated predictions of thermal history and microhardness in laser-deposited Inconel 718 on carbon steel. *Addit. Manuf.* 27, 540–551 (2019).
- Bennett, J. L. et al. Cooling rate effect on tensile strength of laser deposited Inconel 718. Procedia Manuf. 26, 912–919 (2018).
- Yan, Z. et al. Review on thermal analysis in laser-based additive manufacturing. Opt. Laser Technol. 106, 427–441 (2018).
- Johnson, K. L. et al. Simulation and experimental comparison of the thermomechanical history and 3D microstructure evolution of 304L stainless steel tubes manufactured using LENS. Comput. Mech. 61, 559–574 (2018).
- Price, S., Lydon, J., Cooper, K. & Chou, K. Experimental temperature analysis of powder-based electron beam additive manufacturing. In 24th Annual International Solid Freeform Fabrication Symposium, Austin, TX, 162–173 (2013).
- Yang, D., Wang, G. & Zhang, G. Thermal analysis for single-pass multi-layer GMAW based additive manufacturing using infrared thermography. J. Mater. Process. Technol. 244, 215–224 (2017).
- Zhou, S., Dai, X. & Zeng, X. Effects of processing parameters on structure of Nibased WC composite coatings during laser induction hybrid rapid cladding. *Appl. Surf. Sci.* 255, 8494–8500 (2009).
- Popovich, V. et al. Functionally graded Inconel 718 processed by additive manufacturing: crystallographic texture, anisotropy of microstructure and mechanical properties. *Mater. Des.* 114, 441–449 (2017).
- Thomas, A., El-Wahabi, M., Cabrera, J. & Prado, J. High temperature deformation of Inconel 718. J. Mater. Process. Technol. 177, 469–472 (2006).
- Raghavan, N. et al. Numerical modeling of heat-transfer and the influence of process parameters on tailoring the grain morphology of IN718 in electron beam additive manufacturing. Acta Mater. 112, 303–314 (2016).
- Gan, Z. et al. Benchmark study of thermal behavior, surface topography, and dendritic microstructure in selective laser melting of Inconel 625. *Integr. Mater. Manuf. Innov.* 8, 178–193 (2019).
- Rappaz, M. & Gandin, C. A. Probabilistic modelling of microstructure formation in solidification processes. *Acta Mater.* 41, 345–360 (1993).
- Li, S. et al. Melt-pool motion, temperature variation and dendritic morphology of Inconel 718 during pulsed-and continuous-wave laser additive manufacturing: a comparative study. *Mater. Des.* 119, 351–360 (2017).
- Kurz, W. & Fisher, D. Dendrite growth at the limit of stability: tip radius and spacing. Acta Mater. 29, 11–20 (1981).
- Raghavan, A., Wei, H., Palmer, T. & DebRoy, T. Heat transfer and fluid flow in additive manufacturing. J. Laser Appl. 25, 052006 (2013).
- Herriott, C. & Spear, A. D. Predicting microstructure-dependent mechanical properties in additively manufactured metals with machine-and deep-learning methods. Comput. Mater. Sci. 175, 109599 (2020).
- Guo, X., Li, W. & Iorio, F. Convolutional neural networks for steady flow approximation. In Proc. 22nd ACM SIGKDD International Conference on Knowledge Discovery and Data Mining, 481–490 (2016).
- Kim, J. & Lee, C. Prediction of turbulent heat transfer using convolutional neural networks. J. Fluid Mech. 882, A18 (2020).
- Fonda, E., Pandey, A., Schumacher, J. & Sreenivasan, K. R. Deep learning in turbulent convection networks. *Proc. Natl. Acad. Sci. USA* 116, 8667–8672 (2019).
- Abdeljaber, O., Avci, O., Kiranyaz, S., Gabbouj, M. & Inman, D. J. Real-time vibration-based structural damage detection using one-dimensional convolutional neural networks. J. Sound Vib. 388, 154–170 (2017).
- 41. Kiranyaz, S., Ince, T. & Gabbouj, M. Real-time patient-specific ECG classification by 1-D convolutional neural networks. *IEEE Trans. Biomed. Eng.* **63**, 664–675 (2015).
- Abdeljaber, O. et al. 1-D CNNs for structural damage detection: verification on a structural health monitoring benchmark data. *Neurocomputing* 275, 1308–1317 (2018).
- Kiranyaz, S. et al. 1D convolutional neural networks and applications: a survey. Mech. Syst. Signal Process. 151, 107398 (2021).

- Avci, O., Abdeljaber, O., Kiranyaz, S., Hussein, M. & Inman, D. J. Wireless and realtime structural damage detection: a novel decentralized method for wireless sensor networks. J. Sound Vib. 424, 158–172 (2018).
- Yang, D., Pang, Y., Zhou, B. & Li, K. Fault diagnosis for energy internet using correlation processing-based convolutional neural networks. *IEEE Trans. Syst. Man Cybern.*: Syst. 49, 1739–1748 (2019).
- Schirrmeister, R. T. et al. Deep learning with convolutional neural networks for EEG decoding and visualization. *Hum. Brain Mapp.* 38, 5391–5420 (2017).
- 47. Xie, X. et al. Mechanistic data-driven prediction of as-built mechanical properties in metal additive manufacturing. *npj Comput. Mater.* **7**, 1–12 (2021).
- Mahendran, A. & Vedaldi, A. Visualizing deep convolutional neural networks using natural pre-images. Int. J. Comput. Vis. 120, 233–255 (2016).
- Yosinski, J., Clune, J., Nguyen, A., Fuchs, T. & Lipson, H. Understanding neural networks through deep visualization. arXiv:1506.06579 (2015).
- Sui, S. et al. The influence of laves phases on the room temperature tensile properties of Inconel 718 fabricated by powder feeding laser additive manufacturing. Acta Mater. 164, 413–427 (2019).
- Abràmoff, M. D., Magalhães, P. J. & Ram, S. J. Image processing with imagej. Biophotonics Int. 11, 36–42 (2004).
- Wolff, S. J. et al. A framework to link localized cooling and properties of directed energy deposition (DED)-processed Ti-6Al-4V. Acta Mater. 132, 106–117 (2017).
- Vilaro, T., Colin, C. & Bartout, J.-D. As-fabricated and heat-treated microstructures of the Ti-6Al-4V alloy processed by selective laser melting. *Metall. Mater. Trans. A* 42, 3190–3199 (2011).
- Aboulkhair, N. T., Everitt, N. M., Ashcroft, I. & Tuck, C. Reducing porosity in AlSi10Mg parts processed by selective laser melting. Addit. Manuf. 1, 77–86 (2014).
- Li, S., Wei, Q., Shi, Y., Zhu, Z. & Zhang, D. Microstructure characteristics of Inconel 625 superalloy manufactured by selective laser melting. *J. Mater. Sci. Technol.* 31, 946–952 (2015).
- Nie, P., Ojo, O. & Li, Z. Numerical modeling of microstructure evolution during laser additive manufacturing of a nickel-based superalloy. *Acta Mater.* 77, 85–95 (2014).
- Kirkaldy, J., Liu, L. & Kroupa, A. Thin film forced velocity cells and cellular dendrites-II. analysis of data. Acta Mater. 43, 2905–2915 (1995).
- Liu, L. & Kirkaldy, J. Thin film forced velocity cells and cellular dendrites-l. experiments. Acta Mater. 43, 2891–2904 (1995).
- Ge, J., Lin, J., Fu, H., Lei, Y. & Xiao, R. A spatial periodicity of microstructural evolution and anti-indentation properties of wire-arc additive manufacturing 2Cr13 thin-wall part. *Mater. Des.* 160, 218–228 (2018).
- Chen, L. et al. Anisotropic response of Ti-6Al-4V alloy fabricated by 3D printing selective laser melting. *Mater. Sci. Eng.: A* 682, 389–395 (2017).
- Anderson, M., Thielin, A.-L., Bridier, F., Bocher, P. & Savoie, J. δ phase precipitation in Inconel 718 and associated mechanical properties. *Mater. Sci. Eng.: A* 679, 48–55 (2017).
- Kumara, C., Balachandramurthi, A. R., Goel, S., Hanning, F. & Moverare, J. Toward a better understanding of phase transformations in additive manufacturing of Allov 718. *Materialia* 13. 100862 (2020).
- Antonsson, T. & Fredriksson, H. The effect of cooling rate on the solidification of INCONEL 718. Metall. Mater. Trans. B 36, 85–96 (2005).
- Ghosh, S., Stoudt, M. R., Levine, L. E. & Guyer, J. E. Formation of Nb-rich droplets in laser deposited Ni-matrix microstructures. Scr. Mater. 146, 36–40 (2018).
- Ghosh, S. et al. Single-track melt-pool measurements and microstructures in Inconel 625. JOM 70, 1011–1016 (2018).
- Oradei-Basile, A. & Radavich, J. F. A current TTT diagram for wrought alloy 718. Superalloys 718, 325–335 (1991).
- 67. Lindwall, G. et al. Simulation of TTT curves for additively manufactured Inconel
- 68. Stoudt, M. R. et al. The influence of annealing temperature and time on the formation of δ -phase in additively-manufactured Inconel 625. *Metall. Mater. Trans. A* **49**, 3028–3037 (2018).
- Zhang, F. et al. Effect of heat treatment on the microstructural evolution of a nickel-based superalloy additive-manufactured by laser powder bed fusion. *Acta Mater.* 152, 200–214 (2018).
- 70. Kuo, Y.-L., Horikawa, S. & Kakehi, K. The effect of interdendritic δ phase on the mechanical properties of Alloy 718 built up by additive manufacturing. *Mater. Des.* **116**, 411–418 (2017).
- 71. Li, R., Yao, M., Liu, W. & He, X. Isolation and determination for δ , γ' and γ'' phases in Inconel 718 alloy. *Scr. Mater.* **46**, 635–638 (2002).
- Yan, W. et al. Data-driven characterization of thermal models for powder-bedfusion additive manufacturing. Addit. Manuf. 36, 101503 (2020).
- Le, T.-N. & Lo, Y.-L. Effects of sulfur concentration and marangoni convection on melt-pool formation in transition mode of selective laser melting process. *Mater. Des.* 179, 107866 (2019).
- Bennett, J., Glerum, J. & Cao, J. Relating additively manufactured part tensile properties to thermal metrics. CIRP Ann. - Manuf. Technol. 70, 187–190 (2021).

15

- He, X., Yu, G. & Mazumder, J. Temperature and composition profile during double-track laser cladding of H13 tool steel. J. Phys. D: Appl. Phys. 43, 015502 (2009).
- Pratt, P., Felicelli, S., Wang, L. & Hubbard, C. Residual stress measurement of laserengineered net shaping AISI 410 thin plates using neutron diffraction. *Metall. Mater. Trans. A* 39, 3155–3163 (2008).
- Zheng, B., Zhou, Y., Smugeresky, J., Schoenung, J. & Lavernia, E. Thermal behavior and microstructural evolution during laser deposition with laser-engineered net shaping: Part I. numerical calculations. *Metall. Mater. Trans. A* 39, 2228–2236 (2008).
- Zheng, B., Zhou, Y., Smugeresky, J., Schoenung, J. & Lavernia, E. Thermal behavior and microstructure evolution during laser deposition with laser-engineered net shaping: part II. experimental investigation and discussion. *Metall. Mater. Trans. A* 39, 2237–2245 (2008).
- Anisimov, S. I. & Khokhlov, V. A. Instabilities in Laser-matter Interaction (CRC press, 1995).
- Zhang, W. et al. Effect of cooling rates on dendrite spacings of directionally solidified DZ125 alloy under high thermal gradient. Rare Metals 28, 633 (2009).
- Wei, H., Knapp, G., Mukherjee, T. & DebRoy, T. Three-dimensional grain growth during multi-layer printing of a nickel-based alloy Inconel 718. *Addit. Manuf.* 25, 448–459 (2019).

ACKNOWLEDGEMENTS

This work was supported by the National Science Foundation (NSF) under Grant No. CMMI-1934367 and the Beijing Institute of Collaborative Innovation under Award No. 20183405. J.A.G. and J.B. acknowledge support by the US Army Research Laboratory under Grant No. W911NF-19-2-0092. The SEM analysis work made use of the EPIC facility of NUANCE Center and the MatCI Facility of the Materials Research Center at Northwestern University, which was supported by NSF under Grant No. ECCS-1542205 and DMR-1720139, the International Institute for Nanotechnology (IIIN), the Keck Foundation, and the State of Illinois through the IIN.

AUTHOR CONTRIBUTIONS

L.F. conceptualized the study, developed the thermal model, designed the machine learning models, analyzed the results, and wrote the manuscripts and supplementary information. L.C. contributed to the discussion of data-driven models. J.A.G. conducted the SEM microstructure characterization. J.B. performed the DED experiments and

tensile tests. J.C. supervised the DED experiments. GJ.W. supervised the project, co-conceptualized the study, and co-wrote and edited the manuscript. All authors contributed to the discussion of the results and manuscript preparation.

COMPETING INTERESTS

The authors declare no competing interests.

ADDITIONAL INFORMATION

Supplementary information The online version contains supplementary material available at https://doi.org/10.1038/s41524-022-00808-5.

Correspondence and requests for materials should be addressed to Gregory J. Wagner.

Reprints and permission information is available at http://www.nature.com/reprints

Publisher's note Springer Nature remains neutral with regard to jurisdictional claims in published maps and institutional affiliations.

Open Access This article is licensed under a Creative Commons Attribution 4.0 International License, which permits use, sharing, adaptation, distribution and reproduction in any medium or format, as long as you give appropriate credit to the original author(s) and the source, provide a link to the Creative Commons license, and indicate if changes were made. The images or other third party material in this article are included in the article's Creative Commons license, unless indicated otherwise in a credit line to the material. If material is not included in the article's Creative Commons license and your intended use is not permitted by statutory regulation or exceeds the permitted use, you will need to obtain permission directly from the copyright holder. To view a copy of this license, visit http://creativecommons.org/licenses/by/4.0/.

© The Author(s) 2022